AIAA-2009-4021

Controlled Streamwise Vorticity in Diffuser Boundary Layer using Hybrid Synthetic Jet Actuation

Abraham N Gissen*, Bojan Vukasinovic†, and Ari Glezer‡
Woodruff School of Mechanical Engineering,
Georgia Institute of Technology, Atlanta, GA 30332-0405

The formation of streamwise vorticity concentration by exploiting the interaction of surface-mounted passive and active flow control elements with the cross flow is investigated experimentally in a small-scale wind tunnel at high subsonic speeds (up to $M = 0.5$). Controlled formation of streamwise vortices can be a key element in the mitigation of the adverse effects of secondary flows in embedded propulsion system with complex inlet geometries that can affect pressure recovery and distortion at the engine inlet face. The evolution of these vortices is investigated on a converging-diverging insert along one of the test section walls that is designed to provide an adverse pressure gradient that mimics the pressure gradient within a typical offset diffuser. Counter-rotating vortex pairs and single-sense vortices are formed and characterized using conventional passive micro-ramps and micro-vanes, respectively. It is demonstrated that similar streamwise vortices can also be realized using synthetic jet actuators having rectangular orifices that are slanted or skewed to produce single-sense vortices, or streamwise aligned to produce vortex pairs. Hybrid actuation is demonstrated by combining the passive and active actuation approaches to yield a "fail-safe" device with significant degree of controllability.

I. Introduction

Interest in embedded propulsion systems for blended wing body configurations has mandated the development of complex inlet geometries. The evolution of secondary flows at these inlets can result in recovery and flow distortion at the engine face with significant consequences for efficiency (Bansod and Bradshaw, 1972), and these problems are further exacerbated by the ingestion of the boundary layer that forms over the aircraft's wing (Berrier and Allen, 2004). As noted by Daggett et al. (2003), the use of flow control in the inlet of the blended wing body embedded propulsion has the potential for wide reaching system level performance improvements.

A significant body of work has demonstrated that the secondary flows and separation in complex inlet ducts can be mitigated by induced concentrations of streamwise vorticity on the internal flow surfaces. Passive vortex generators (e.g., vanes) have been successfully applied in embedded inlets to improve inlet recovery and reduce pressure distortion. In a study by Anderson and Gibb (1993) a row of vane type vortex generators in an s-duct was found to reduce distortion and increase pressure recovery at the exit plane of the inlet. The reduction of the distortion effects induced by the ingestion of a thick boundary layer by using vane arrays was investigated by Anabtawi et al. (1999). More recently, Anderson et al. (2002) have demonstrated in a numerical study the control effectiveness of passive vane type vortex generators having a

* Graduate Research Assistant, AIAA Member.
† Research Engineer, AIAA Member.
‡ Professor, AIAA Associate Fellow.

characteristic cross stream scale that was selected to be a fraction of the boundary layer height to reduce losses. In a later numerical investigation, Anderson et al. (2004) showed that small-scale (“micro”) vanes can be used to reduce pressure distortion at the exit plane of compact s-ducts. Experimental work by Jirásek (2006) on complex, D-throat, heavily serpentined inlets further corroborated the efficacy of sub-boundary layer vane actuators. Tournier et al. (2005) used two rows of vane type vortex generators to produce arrays of single-sense streamwise vortices in an offset diffuser at $M = 0.6$ with deliberately-imposed inlet distortions, and reported marked improvements in pressure distortion at the exit plane. Owens et al., (2008) used a single row of vortex generators in an s-duct operating in a free stream at $M = 0.85$ resulting in reduction of circumferential distortion levels at the engine face. Sub-boundary layer passive flow control devices (micro-ramps) for controlling shock wave boundary layer interactions were investigated via experimentally validated numerical computations by Anderson et al. (2006) in a supersonic inlet. These authors reported that these vortex generators significantly reduced the interactions and their unsteady effects on the outer flow field. Micro-ramps similar to those used by Anderson et al. (2006) were also investigated experimentally by Babinsky et al. (2009) who showed performance gains in terms of reduced shock-induced separation. However, the distinct advantages offered by passive vortex generators are offset by the inherent pressure losses, and by the lack of spatial and temporal adjustability of the ensuing streamwise vortices which makes it hard to optimize their performance over a broad flight envelope.

Active flow control approaches that rely on distributions of normal and skewed jets emanating from the inner surfaces of the inlet duct have provided significant improvement in the performance of s-ducts. With the potential for rapid actuation and little drag penalty in the absence of actuation, this active flow control approach is very attractive for controlling the flow within an s-duct. Anderson et al., (2004) preformed a DOE analysis to optimize the use of skewed jets with significant improvements in pressure recovery and engine face distortion. Scribben et al. (2006) used vortex generator jets in a complex serpentine inlet duct and showed drastic improvements in distortion levels and a small reduction in drag. In similar experiments, Owens et al. (2008) used various arrays of vortex generator jets in a serpentine inlet at $M = 0.85$ to gain insight into optimal design. Recently, Amitay et al. (2008) explored the utilization of synthetic (zero mass flux) jets for controlling flow separation in an offset duct and reported partial flow reattachment. It is noteworthy that while active actuation approaches can be adapted to provide feedback control in flight, the system can be complex, often requires significant engine bleed, and is not completely fail-safe.

In combining active and passive flow control (hybrid flow control) Owens et al. (2008) used micro-vanes and micro-jets to improve the performance of a serpentine inlet duct across a broad range of flow rates especially at low velocities for which the micro-vanes were not optimized. In an effort to reduce the engine bleed required, Anderson et al. (2009) combined the micro-ramps used in his earlier work (Anderson et al. 2006) with flow injection resulting in an almost 10-fold reduction in required engine bleed.

The present paper focuses on the characterization of the interaction of passive and active vortex generators with the cross flow within a high-speed subsonic duct in the presence of an adverse pressure gradient that is representative of the flow in an offset diffuser. Specific emphasis is placed on details of the roll up and far-field evolution of single-sense and counter-rotating pairs of streamwise vortices. Passive vortex generators include micro-vanes and micro-ramps, while active vortex generators are based on surface-embedded synthetic jet actuators where variations in the orifice geometry are used to create either single or pairs of streamwise vortices. The synthetic jet actuators are used to augment the passive elements in hybrid configurations with a broader, controllable operating range and an inherent fail-safe margin. The use of synthetic (zero mass flux) jet actuators obviates the need for supply of bleed air and therefore of complex fluidic plumbing and integration.

II. Experimental Setup and Procedures

The experiments are performed in a small, open-return pull-down high-speed subsonic wind tunnel (test sections speeds of up to $M = 0.75$), and driven by a 150 HP blower. The modular test section (Figure 1) measures 12.7 × 12.7 × 61 cm, and the temperature of the return air is controlled using a chiller coupled with an ultra low pressure drop heat exchanger. The upper wall of the test section is fitted with a converging-diverging insert to impose an adverse pressure gradient of $dp/dx \approx 0.38 \cdot p_s/L$ which closely matches the pressure gradient in a typical offset diffuser.

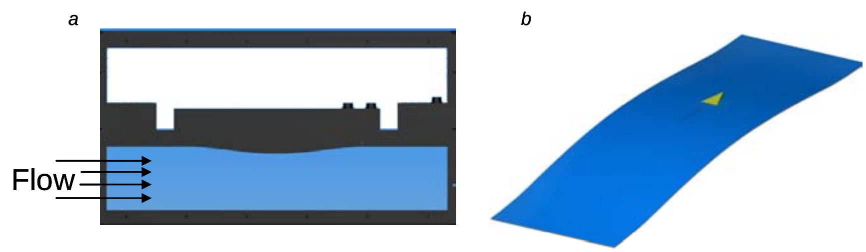

Figure 1. *Test section schematics of the transonic wind tunnel (a) and converging-diverging wall (b).*

Various passive (micro-ramp and micro-vane) and active (synthetic jet) flow control actuators are surface mounted near the apex of the converging-diverging test section insert for characterization of the induced streamwise vortices. Schematic descriptions of the various devices are shown in Figure 2 (where the streamwise position is measured relative to the wall apex). The characteristic scaling of the passive devices relative to the boundary layer thickness δ ($\delta = 5$ mm at the apex at $M = 0.5$) are based on the DOE study of Anderson et al. (2004, 2006). The micro-vane (Figure 2*a*) has a rectangular planform measuring $0.25\delta \times 2.56\delta$ in the cross-stream and streamwise directions at $\varepsilon = 8°$ relative to the free stream, and the micro-ramp (Figure 2*b*) is 0.51δ high, 3δ in wide, and 3.4δ long, and has a half-angle of 24°. The synthetic jet orifices measure 24.9 × 0.5 mm and can operate within the range 1-2.5 kHz. The slanted jet (Figure 2*c*) is aligned with the micro-ramp, while the streamwise jet (Figure 2*d*) is aligned with the free stream (both issues normal

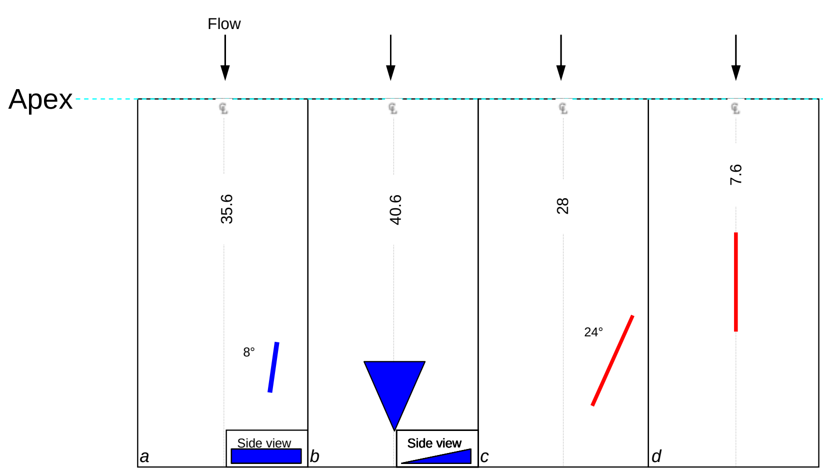

Figure 2. *The configuration of each flow control elements and : a) micro-vane, b) micro-ramp, and c) slanted, d) streamwise The distance of each element from the surface apex is marked (in mm).*

to the surface). In addition, a hybrid configuration (Figure 4) is comprised of the micro-ramp with the streamwise jet along its centerline (orifice's downstream edge is 8mm upstream of the ramp).

The present synthetic jets are calibrated using simultaneous, phase-locked measurements of the jet exit velocity, piezoelectric disk (centerline) displacement and cavity pressure and temperature. Figure 3*a* shows the schematics of the calibration-fitted actuator. Calibration data are shown in Figure 3*b* in terms of the jet Strouhal number $St = f_d \cdot \zeta / U_j$, where f_d is the driving frequency, ζ is the disk displacement amplitude, and U_j is the jet average velocity during the expulsion cycle. Two operating regimes are identified in Figure 3*b*: first, at the low operating voltage and a given frequency, exit jet velocity approximately scales with $f_d \cdot \zeta$. As the applied voltage increases, St approaches a second limit in which $p/\rho U_j^2$ is approximately constant and the jet velocity is proportional to the cavity pressure. It should be noted that the $p/\rho U_j^2$ is a complex function of the actuator geometry and disk displacement. In the present measurements the operating frequency is 2.2 kHz and time-averaged jet speed (over the blowing cycle) is U_j = 37 m/s.

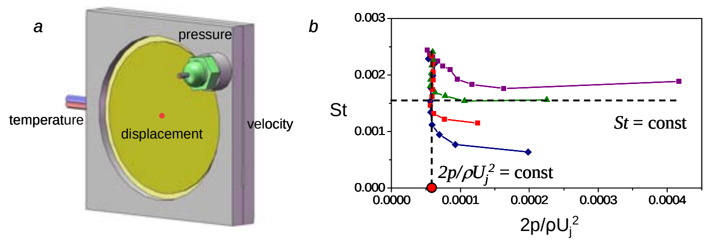

Figure 3. *a). Multi-parameter calibration of the synthetic jet actuator and b). The calibration results for the operating frequencies f = 1600 (♦), 1400 (■), 1200 (▲), and 1000 (■) Hz.*

Diagnostics include high-resolution, high-speed PIV measurements at multiple cross stream (*x-y*) *z*-planes of the flow fields. The PIV field of view measures 17 mm on the side and the magnification is 17 μm/pixel. The outline of the PIV measurement stations are shown in Figure 4 (using the hybrid configuration): near-field measurements are take at centerspan (marked "1", where the PIV view is comprised of four partially-overlapping streamwise fields). Far-field measurements are taken at x/δ_{apex} = 42 downstream of the micro-ramp's downstream edge at cross-stream planes 1 mm apart.

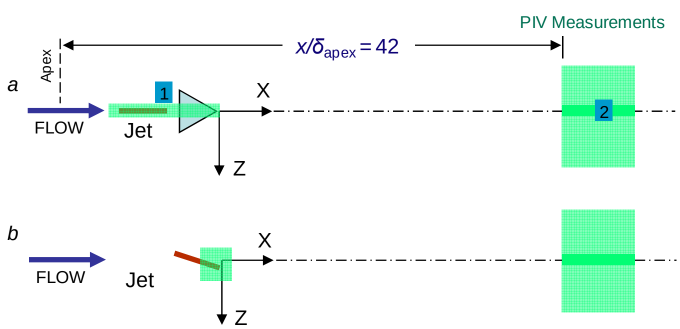

Figure 4. *Schematics of the three PIV measurement domains for the hybrid flow control (a) and slanted-jet active flow control (b).*

III. Results

III.1 Passive Formation of Streamwise Vortices

The single-sense and counter-rotating streamwise vortices induced by the micro-vane and micro-ramp (cf. Section II) are characterized in the adverse pressure gradient domain downstream of the wall apex (Figure 1). The initial vortex formation by the two passive elements was investigated using surface oil visualization using a mixture of linseed oil and titanium-dioxide paint. The oil traces around the micro-vane (Figure 5*a*) indicates stagnation points upstream and downstream of the vane's leading and trailing edges, respectively. The pressure differential across the vane's surfaces leads to the rollup of a "tip vortex" which rolls to form a single-sense streamwise vortex. The oil streak accumulation downstream from the trailing edge of the vane indicates roughly an upwash region across the boundary layer. Figure 5*b* shows the near-wall topology of the flow over the microramp and initial vortex formation. Symmetric split of the oncoming flow over the microramp is visualized, and the footprint of initial streamwise roll of the flow is evident from the wall traces on each side of the ramp. As more fluid rolls into each streamwise vortex that forms along the micro-ramp's edge, its footprint on the ramp side wall intensifies. The evolving CCW and CW vortices (in the downstream view) that form along the left and right edges of the micro-ramp, respectively merge at its tip and are advected downstream within the boundary layer as is evident from the two narrow traces about the micro-ramp's axis. It should be noted that these traces are not a normal projection of the vortex cores, but rather delineate the upwash due to the vortex-induced spanwise flow. The vortex pair self-advects away from the surface as is evidenced by the streamwise thinning of the upwash traces although their streamwise evolution is clearly dominated by primary (streamwise) flow.

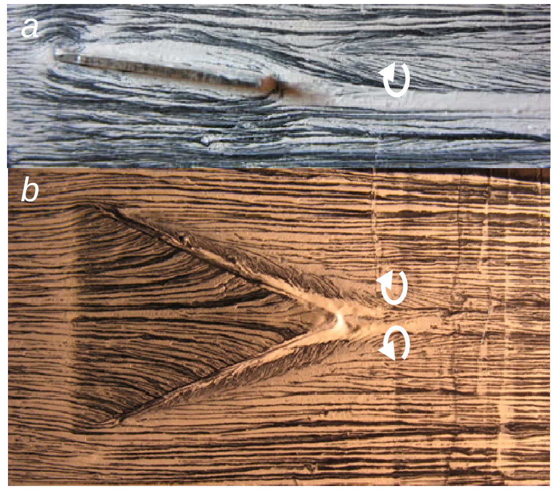

Figure 5. *Surface oil-flow visualization of the streamwise single-sign (a) and vortex pair (b) formation.*

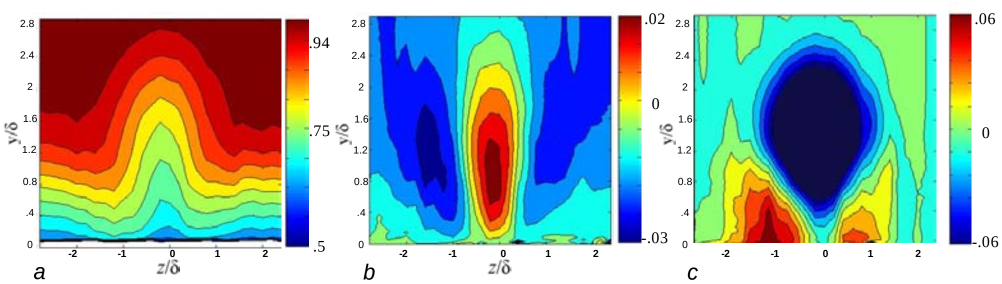

Figure 6. *Color raster plots (with contours) of composite, time-averaged streamwise (U, a) and cross stream (V, b) velocity distributions in the cross-stream y-z plane at $x/\delta_{apex} = 42$ showing the effects of the micro-ramp. Contours of the streamwise velocity difference (in the presence and absence of the vane) are shown in c. The z-y plane is viewed in the upstream direction.*

The far-field ($x/\delta_{\mathrm{apex}} = 42$, δ_{apex} is the boundary layer thickness at the apex) effect of the micro-ramp on the boundary layer is elucidated from a sequence of planar PIV measurements in cross stream planes at a number of spanwise stations (cf. Figure 4*a*). A color raster plot (with contours) of composite time-averaged streamwise and cross stream velocity distributions in the *y*-*z* plane are shown in Figures 6*a* [$U(y,z;x)$] and b [$V(y,z;x)$], respectively. These distributions indicate a clear upwash effect at center span (the centerline of the micro ramp) which is accompanied by the downwash domains with peaks at $z/\delta_{\mathrm{apex}} = +5$ and -5 on both sides of the upwash. These effects are a direct consequence of the induced counter-rotating vortex pair off the ramp. To better isolate the effect of the streamwise vortex, the streamwise velocity increment (decrement) relative to the baseline flow (in the absence of actuation) $\Delta U(y,z;x)$ is shown in Figure 6*c*. Inspection of Figure 6*c* indicates that the deficit caused by the common upwash of the vortices is advected upward introducing higher speed flow in the near wall region. Note that a slight bias in the PIV measurements (in which the boundary layer appears slightly inclined) in the absence of the micro-ramp is caused by a slight misalignment between the PIV camera horizon and the wall contour.

A cross-stream integral effect of the micro-ramp on the boundary layer flow is assessed from the relative spanwise changes in the shape factor *h* of the cross stream velocity distribution in the absence and presence of the micro-ramp element (Figure 7). These data show that the spanwise extent of the micro-ramp is almost $5\delta_{apex}$, while the micro-ramp width is about $3\delta_{apex}$. The most prominent feature of *h*(z) is that the induced streamwise vortices lower the shape factor through most of the affected spanwise domain. Even though the upwash along the micro-ramp's centerline increases the boundary layer velocity deficit (Figure 6), the vortex pair is sufficiently far from its source, such that its lift off the wall actually leads to a decrease of the velocity deficit near the wall. In the downwash region, the transport of high-momentum fluid towards the surface leads to an increase in the velocity deficit near the wall. The combination of off-centerline downwash and displaced upwash in between is what makes the microramp attractive (when properly scaled) for boundary layer separation delay (Lin, 2002).

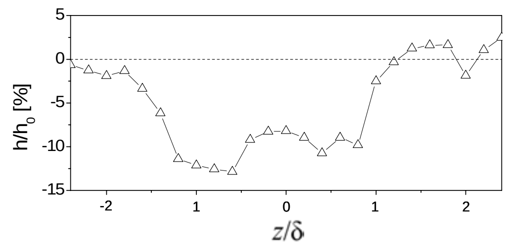

Figure 7. *Spanwise distribution of the bl shape factor h downstream of the micro-ramp (x/δapex=42) normalized by the baseline shape factor h_0 (Figure 4a).*

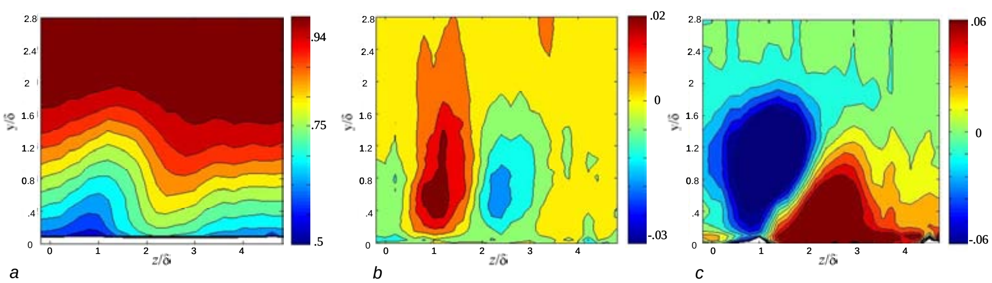

Figure 8. *Same as Figure 6 for a micro-vane.*

Similar to Figure 6, the changes in the flow field that are induced by a micro-vane are measured at $x/\delta_{apex} = 42$ and are shown in color raster plots in Figures 8*a* and *b*. The time-averaged distribution of the streamwise velocity *U*(*y*,*z*;*x*) (Figure 8*a*) shows the upwash ($0.5 < z/\delta_{apex} < 2$) and downwash ($2 < z/\delta_{apex} < 3$) domains indicating the presence of a CW streamwise vortex. This is further supported by the distribution of the cross-stream velocity (Figure 8*b*), that includes two adjacent zones of fluid motion either away (upwash) or towards (downwash) the wall. As might be expected, owing to the presence of the wall, the cross stream elevations of the peaks (positive and negative) of ΔU (Figure 8*c*) are different. The deficit owing to the upward advection of low-momentum fluid (at $y/\delta_{apex} \approx 1.2$) is farther away from the surface than the high-momentum fluid (at $y/\delta_{apex} \approx 0.4$) and in fact, the transported high-momentum concentration appears to spread in

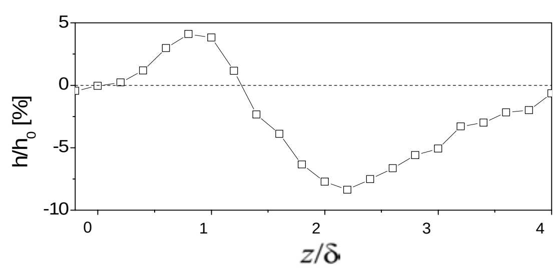

Fiaure 9. *Same as Fiaure 7 for a micro-vane.*

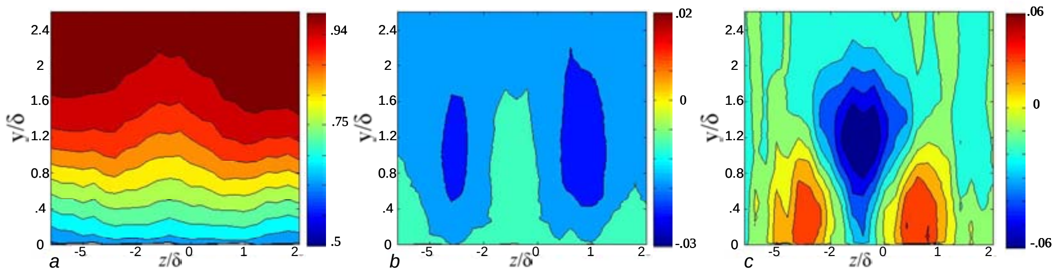

Figure 10. Same as Figure 6 for a streamwise synthetic jet.

the spanwise direction along the surface. It is noteworthy that the upwash in absence of an opposite-sense vortex is not sufficient to displace the low momentum fluid away from the surface indicating that the effectiveness of the micro-vane in terms of overcoming flow distortion and separation may be somewhat lower than that of the micro-ramp.

This is further confirmed by the distribution of the shape factor $h(z)$ across the span (Figure 9). In comparison to the corresponding distribution for the micro-ramp, the domain in which $h(z)$ increases is considerably broader. However, considering that the spanwise projection of the micro-vane is about $0.4\delta_{apex}$ compared to $3\delta_{apex}$ for the micro-ramp, indicates that perhaps comparable effects can be achieved by increased packing density of the micro-vanes.

III.2 Formation of Streamwise Vortices using Synthetic Jet Actuation

One of the objectives of the present work is to investigate the utility of synthetic jets for controlled formation of counter-rotating or single-sense streamwise vorticity concentrations. A pair of counter-rotating streamwise vorticies is produced by aligning the long dimension of the rectangular jet orifice (cf. Figure 2) with the direction of the free stream. In still air the rectangular jet generates a pair of counter rotating vorticies along the orifice at each actuation cycle. In the presence of a cross flow, these vortices are augmented by the tilting and rollup of boundary layer (predominantly spanwise) vorticity and may be loosely connected at their downstream end (similar to a lambda vortex). These vortices which are advected with the local cross flow are clearly interrupted and vanish during the suction stroke. Because the strength of the streamwise vortices that are formed by a synthetic jet actuator is streamwise modulated with the periodicity of the actuation, their time-averaged strength is considerably weaker than their instantaneous strength. A streamwise vortex pair induces an upwash along its common axis and a downwash off centerline. The resulting changes in the baseline flow are shown in Figure 10 using color raster plots of the time-averaged streamwise and cross stream velocity components. As expected, when the streamwise jet is active (Figure 10*a*), there is a noticeable upwash near the centerline peak in boundary layer thickness, and is flanked on either side by weaker downwash where the high speed flow is drawn closer to the wall. Similar to Figure 6*c*, the distributions of the streamwise velocity differences relative to the unforced flow (in the absence of actuation) $\Delta U(y,z;x)$ are shown in Figure 10*c*. These data indicate that the time-averaged flow induced by the synthetic jet is qualitatively similar to the far-field structure of the flow induced by the micro-ramp (cf. Figures 6). The shape factor is shown in Figure 11 and indicates that while the

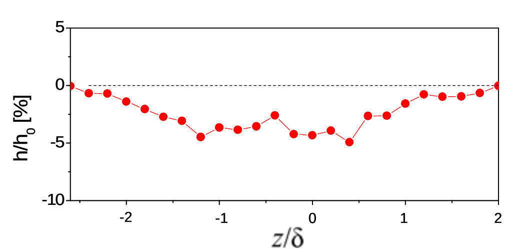

Figure 11. Same as Figure 7 for a micro-vane.

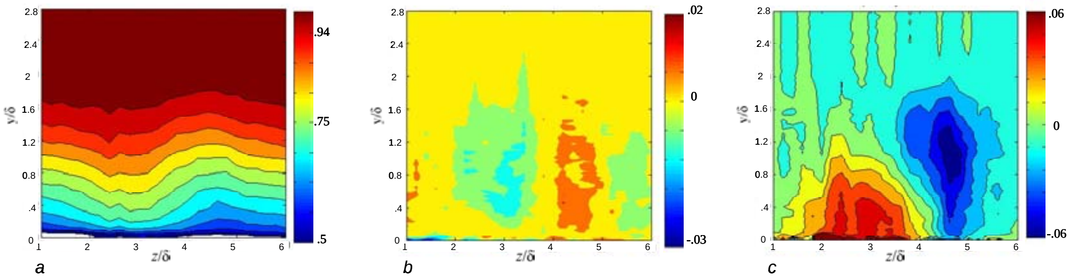

Figure 12 Same as Figure 6 for a slanted synthetic jet.

streamwise jet leads to an overall decrease in the shape factor, the magnitude of the decrease is smaller than what is induced by the micro-ramp. While it might be argued that the jet momentum (or impulse per stroke) affects the strength of the induced streamwise vortices, it appears that for a given velocity ratio (to the free stream), the strength of the ensuing streamwise vortices is affected by the characteristic spanwise scale of the jet. In the present configuration while spanwise domain of influence of the jet is similar to that of the micro-ramp (about $5\delta_{\mathrm{apex}}$), the spanwise width of the jet is about 30 times smaller that that of the ramp ($0.1\delta_{\mathrm{apex}}$ compared to $3\delta_{\mathrm{apex}}$).

A single streamwise vortex (similar to the micro-vane) is generated by slanting the orifice of the jet relative to the free stream (cf. Figure 2*c*). The jet slant angle is selected to be the same as the half apex angle of the micro-ramp. The resulting flow in the far field is shown in Figure 12 and indicates the presence of a CCW streamwise vortex. Unlike the streamwise jet the low speed flow that is pushed out away from the wall is not convected upward quite as strongly which leads to areas of both increased and decreased velocity deficits in the near wall region (as also illustrated by the raster plot of the velocity difference in Figure 12*c*). It is noted that although the synthetic jet is slanted at the same direction as the micro-vane (see Figure 2) they generate single streamwise vortices of opposite sense. While the vortex that is formed by the vane is similar to a tip vortex of a lifting surface, the vortex that is formed by the jet appears to roll as a result of the bending of the jet by the cross flow as shown by Peake et al. (1999) for continuous (conventional) jets and is consistent with the measurements of Compton and Johnson (1992) for skewed jets. The near-field formation of the vortex that is generated by the slanted jet was measured in 16 cross stream (y-x) planes 1 mm apart where the field of view measures 17 × 17 mm beginning at $x/\delta_{apex} = 2$ downstream of the upstream orifice edge (cf. Figure 4). The resulting rendition of a 3-D composite of near-field flow is shown in Figure 13. Figure 13*a* shows surfaces of the cross stream velocity. The presence of the jet forces the oncoming flow up away from the surface along the jet orifice and induces a downward flow in a domain that is outboard and downstream from the

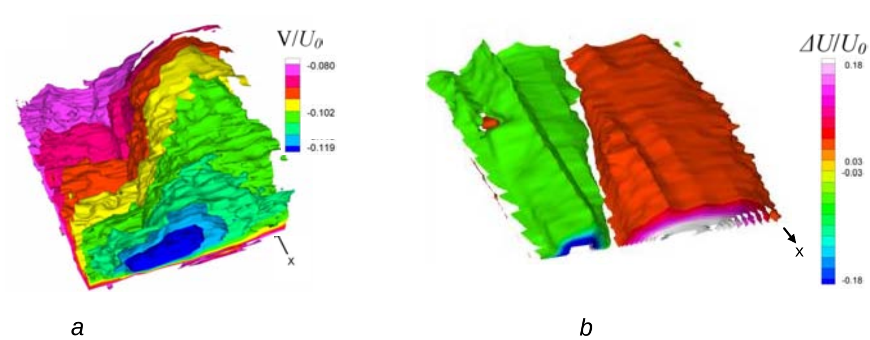

Figure 13. *Rendition of the composite 3-D time-averaged velocity field downstream of the slanted synthetic jet showing surfaces of V (a) and ΔU (b). The view is upstream.*

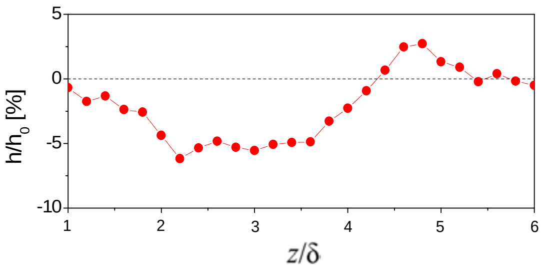

***Figure 14**. Same as Figure 7 for a slanted synthetic jet.*

jet orifice. The bending of the jet by the cross flow is evident in surfaces of the streamwise velocity difference (relative to the baseline flow) as shown in Figure 13*b* and is accompanied by an increase in the streamwise velocity on the right (downstream of the orifice) and a small decrease owing to the flow turning on the left. Clearly, the differences in the sense of the streamwise vortices that are formed by slanted passive obstructions and by similar-slant synthetic jets must be taken into consideration in the design of hybrid actuators that are comprised of both elements.

The spanwise distributions of the changes in the shape factor that are effected by the slanted jet are shown in Figure 14. It is remarkable that the spanwise extent of the changes in shape factor that are induced by the slanted jet and by the microvane (Figure 9) are quite similar (approximately $3\delta_{apex}$) in the far field. The streamwise projection of the vane is $.5\delta_{apex}$ and the streamwise projection of the jet is $2\delta_{apex}$. Furthermore, the magnitude of the effect of the jet is only about 15% lower based on the averaged change in shape factor.

III.3 Hybrid Formation of Streamwise Vortices

Initial tests of a "hybrid" actuator that comprises a vortex generator and synthetic jets were conducted using a streamwise jet placed upstream of a micro-ramp along its centerline (cf. Figure 2*d*). This configuration was motivated by the successful integration of a conventional continuous jet and a micro-ramp by Anderson (Anderson et al. 2009). Measurements of the velocity distribution in overlapping cross stream planes were acquired phase-locked to the actuation wave form at eight instances during the actuation cycle at $\Delta\phi = 45°$ apart. Three of the resulting composite flow fields are shown in Figure 15, at the beginning ($\phi = 0°$, Figure 14*a*) and end ($\phi = 180°$, Figure 15*b*) of the expulsion cycle, and at the peak of the suction cycle ($\phi = 270°$, Figure 15*c*) of the jet actuator. Figure 15*a* shows the vorticity concentration within the boundary layer upstream of the ramp and the separation domain and free shear layer that form downstream of the ramp. It is noteworthy that the upwash induced by the ramp's two counter-rotating vortices on the centerline results in the deficit of the streamwise velocity above the wall layer on top of the ramp as is evident by the "streak" of streamwise vorticity there. At the end of the current expulsion cycle (Figure 15*b*), the ejected jet fluid clearly displaces the local boundary layer and the jet-induced streamwise vortices lead to an upwash that is manifested by the deficit in the streamwise velocity above the surface upstream of and along the ramp. These distortions

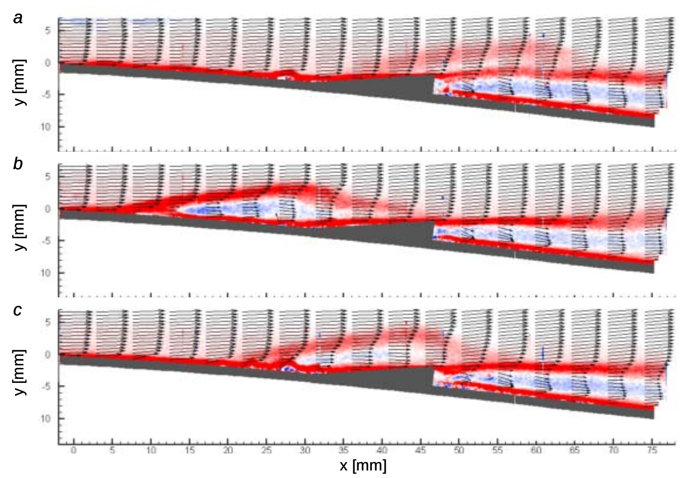

***Figure 15.** Contour plots of the phase-averaged vorticity with overlaid velocity profiles at the beginning of the jet expulsion cycle (a), end of the expulsion cycle (b), and at the peak of the suction cycle (c) of the actuation period. measured at the PIV domain (1) (Figure 4).*

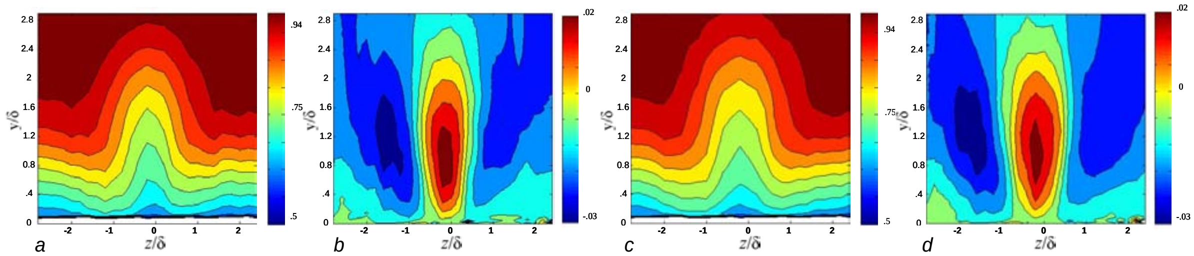

Figure 16*. Same as in Figure 6: U (a and c), and V (b and d) for a "hybrid" micro-ramp and synthetic jet: (a-b) micro-ramp alone, and c-d) micro-ramp and jet .*

appear as a local shear layer with concentrations of spanwise vorticity. It is noteworthy that at this streamwise position, the upwash effects of the jet and ramp streamwise vortices appear to be comparable (based on the induced velocity deficit). At the peak of a suction cycle (Figure 15*c*), the effect of the jet appears to be some blockage which interacts with the shear layer above the micro-ramp. These measurements clearly indicate that in addition to the continuous vorticity flux associated with the rollup of the ramp's vortices, the jet actuator introduces time-varying manipulation of the boundary-layer vorticity, which is advected atop of the micro-ramp and begins to interact with the "primary" streamwise vortices downstream from its trailing edge.

The far-field effects of the micro-ramp were discussed in connection with Figure 6. Distributions of the time averaged *U* and *V* downstream of the ramp in the absence and presence of the jet are shown in Figure 16. These data clearly show the central upwash domain and two downwash regions on either side. These data indicate that the time-averaged effect of the jet in this configuration is somewhat limited and there is a slight enhancement of both the upwash and downwash. As for the individual actuation by the vortex generators and the jets, the spanwise effect of the hybrid actuation is assessed from spanwise distributions of the shape factor (Figure 17). These data show that the percent of additional changes in the shape factor (relative to the shape factor in the presence of the ramp) when the jet is activated are somewhat smaller than the percent changes induced by the jet alone (relative to the baseline boundary layer, Figure 7).

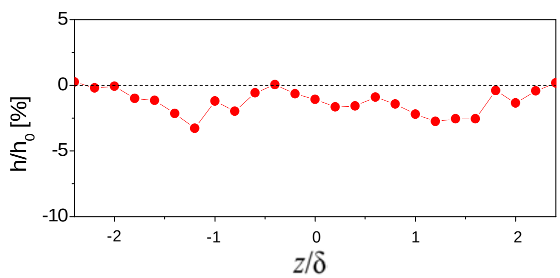

Figure 17. *The shape-factor distribution for the hybrid control (h) relative to the passive (h_0) control across the span in the far-field domain (Figure 4a).*

As noted above, the instantaneous changes induced by the jets can be larger than the time-averaged changes. Compared to exclusive passive control, the jet adds a dynamic component at the actuation frequency to the manipulation of the boundary layer vorticity. The assessment of the dynamic effect in the far field is done using phase-averaged measurements [at the measurement station (2) in Figure 4]. Similar to the near field, the phase-locked measurements are taken at eight equally-spaced phase increments ($\Delta\phi = 45°$). Six cross-stream distributions of the phase-locked streamwise and cross stream velocities and the rms fluctuations are shown in Figure 18*a-c*, respectively, along with corresponding time-averaged distributions in the absence of the jet (i.e., passive element only). These data show that even in the far field, the flow preserves the time periodic effect of the jet. Substantial variation in shape of the instantaneous velocity distributions induces temporal increase and decrease in the downwash of the flow. However, as evidenced by predominant reduction in near-wall velocity deficit in the streamwise direction (Figure 18*a*) and the accompanying increase in the cross-stream (Figure 18*b*) velocity component, the overall effect of simultaneous active and passive actuation can enhance the effects of the actuation on the boundary layer by the added dynamic fluctuation of the boundary layer vorticity. Recent numerical investigations by Lakebrink et al (2009) indicate that once the jet actuation is added to the micro-ramp, the two counter-rotating vortices that are formed off the micro-ramp become dynamically modulated, which destabilizes the boundary layer in the spanwise direction and leads to the formation of additional streamwise vortices. These findings suggest that the synthetic jet actuation enhances the primary effect of the micro-ramp by "triggering" the formation and spanwise spreading of secondary streamwise vortices.

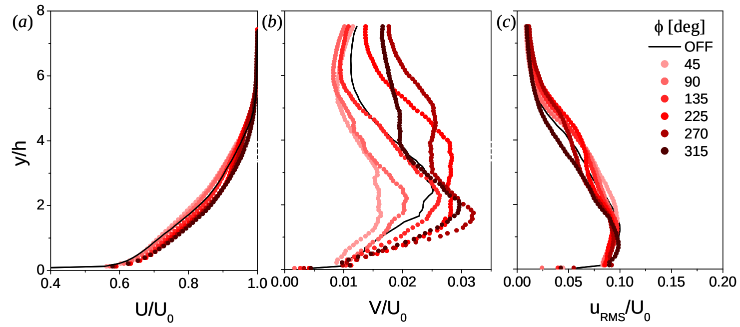

Figure 18. *Mean streamwsie (a) and cross-stream (b) velocity profiles and the corresponding RMS velocity fluctuations (c) for the baseline (***—***) and actuated flow at six phases of the actuation cycle, measured at the PIV domain (2) (Figure 4).*

The dynamic nature of the boundary layer manipulation is further characterized by calculation of phase-averaged shape factors based on the streamwise velocity distributions in Figure 18*a*. The variation of the shape factor with the phase of the actuation cycle is shown in Figure 19*a*. Continuous variation of the boundary layer shape factor during one actuation period induces a net reduction in the shape factor which remains *lower* than in the baseline (i.e., passive control) for most of the actuation period. The peak additional reduction in *h* is about 3%, and the overall reduction is estimated to be about 1.2%.

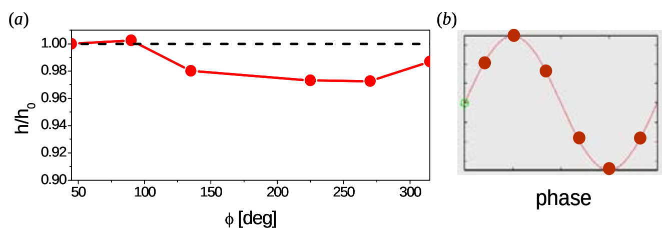

Figure 19. *a) Phase variation of the shape factor (●) based on the velocity distributions in Figure* ***18****, and. b) Illustration of the corresponding phase-points during the actuation cycle.*

IV. Conclusions

The present work has focused on an experimental investigation of the formation of streamwise vorticity concentration by exploiting the interaction of passive and active flow control elements with the cross flow. The evolution of these vortices is investigated on a converging-diverging insert in a small-scale wind tunnel that is designed to provide an adverse pressure gradient which mimics the pressure gradient within a typical offset diffuser. Counter-rotating vortex pairs and single-sense vortices are formed and characterized using conventional passive micro-ramps and micro-vanes, respectively.

Single-sense and pairs of counter-rotating vortices that are advected within the wall boundary layer are formed using passive flow elements based on a micro-vane and a micro-ramp, respectively. It is shown that the induced motion by the counter-rotating vortex pair that is formed by a micro-ramp leads to its slow lifting off the surface with significant displacement of the velocity deficit that is associated with upwash while a local downwash transports high-speed fluid to the vicinity of the surface. A single-sense vortex produced by a micro-vane induces a downwash on one side and an upwash (which does not lift off the surface) on the other which persist across the span in the far field. It is also shown that unsteady single and counter rotating pairs of streamwise vortices can be actively formed by streamwise and slanted synthetic jet configurations, respectively. The jet-produced vortices are temporally segmented at the actuation frequency of the jet and while their time-averaged interactions with the base flow (as may be measured by spanwise variation of the boundary layer shape factor) is somewhat weaker than that of the corresponding nominally-steady passive vortex generators, their instantaneous effects may be significant. It is also noteworthy that owing to differences in the interaction mechanism with the boundary layer between the synthetic jet and the micro-vane, the single streamwise vortex that is formed by a slanted synthetic jet has the opposite sense than the vortex generated by a micro-vane having the same slant orientation.

Finally, preliminary integration of passive and active control element into a hybrid actuator element is demonstrated by using a streamwise synthetic jet which is symmetrically aligned upstream of a microramp. The objective is to augment the counter-rotating vortex pair generated by the microramp exploiting the additional counter-rotating vortex pair that is formed by synthetic jet actuator just upstream from the microramp. The results indicate that the integration improves on the effectiveness of the passive control and, furthermore, numerical simulations suggest that the unsteady modulation of the streamwise vortices that are induced by the passive elements can lead to spanwise spreading of the streamwise vortices.

Acknowledgment

This work has been supported by NASA and the Boeing Company.

The authors are grateful to Dr. Anderson, Dr. Mace, Dr. Mani, Ms. McMillan, and Mr. Lakebrink for a number of insightful discussions.

References

Amitay, M., Pitt, D., Glezer, A. "Separation Control in Duct Flows," *J. Aircraft*., **39**, 616-620, 2008.

Anabtawi, A.J., Blackwelder, R.F., Lissaman, B.S.P, Liebeck, R.H. "An Experimental Investigation of Boundary Layer ingestion in a Diffusing S-Duct With and Without Passive Flow Control," AIAA Paper 1999-0739, 1999.

Anderson, B.H., Gibb, J. "Study on Vortex Generator Flow Control for the Management of Inlet Distortion," *J. Prop. Pow*., **9**, 422-430, 1993.

Anderson, B.H., Baust, D.H., Agrell, J. "Management of Total Pressure Recovery, Distortion and High Cycle Fatigue in Compact Air Vehicle Inlets," NASA/TM. 2002-212000.

Anderson, B.H., Miller, D.N., Addington, G.A., Agrell, J. "Optimal Micro-Vane Flow Control for Compact Air Vehicle Inlets," NASA/TM. 2004-212936.

Anderson, B.H., Miller, D.N., Addington, G.A., Agrell, J. "Optimal Micro-Jet Flow Control for Compact Air Vehicle Inlets," NASA/TM. 2004-212937.

Anderson, B., Tinapple, J., and Surber, L. "Optimal Control of Shock Wave Turbulent Boundary Layer Interactions Using Micro-Array Actuation," AIAA Paper 2006-3197, 2006.

Anderson, B.H., Mace, J.L., Mani, M. "Active "Fail Safe" Micro-Array Flow Control For Advanced Embedded Propulsion Systems," AIAA Paper 2009-741, 2009.

Babinsky, H. Li, Y., Pitt., Ford, C.W. “Optimal Microramp Control of Supersonic Oblique Shock-Wave/Boundary-Layer Interactions,” *AIAA J.*, **47**, 668-675, 2009.

Bansod, P., Bradshaw, P. “The Flow in s-shaped Ducts,” *Aeronaut. Q.*, **23**, 131-140, 1972.

Berrier, B.L., Allan, B.G. “Experimental and Computational Evaluation of Flush-Mounted, S-Duct Inlets,” AIAA Paper 2004-764, 2004.

Daggett, D.L., Kawai, R, Friedman, D. “Blended Wing Body Systems Studies: Boundary Layer Ingestion Inlets With Active Flow Control,” NASA/CR 2003-212670.

Jirásek, A. “Development and Application of Design Strategy for Design of Vortex Generator Flow Control in Inlets,” AIAA Paper 2006-1050, 2006.

Lakebrink, M.T., Mani, M., Mace, J.L., McMillan, M.L. “Numerical Investigation of Fluidic Hybrid Flow Control Influence on Boundary Layer Characteristics,” AIAA Paper 2009-2407, 2009.

Lin, J.C. “Review of research on low-profile vortex generators to control boundary-layer separation,” *Progress in Aerospace Sciences*, **38**, 389-420, 2002.

Owens, L.R., Allan, B.G., Gorton, S.A. “Boundary-Layer-Ingesting Inlet Flow Control,” *J. Aircraft*., **45**, 1431-1440, 2008.

Peake, D.J., Henry, F.S., and Pearcey, H.H.,“Viscous Flow Control with Air-Jet Vortex Generators,” AIAA Paper 1999-3175, 1999.

Scribben, A.R., Ng, W., Burdiso, R. “Effectiveness of a Serpentine Inlet Duct Flow Control Technique at Design and Off-Design Simulated Flight Conditions Design of the Blended Wing Body Subsonic Transport,” *J. Turbomachinery*., **41**, 333-339, 2004.

Tournier, S., Paduano, J.D. “Flow Analysis and control in a Subsonic Inlet,” AIAA Paper, 2005-4734, 2005.